Research Article | Vol. 2, No. 11 / 15 November 2019 / OSA Continuum 3037

Broadband telecom emission from InP/InGaAs nano-ridge lasers on silicon-on-insulator substrate

Wai Kit Ng,[1] Yu Han,[2] Kei May Lau,[2,3] and Kam Sing Wong[1,4]

[1]*Department of Physics, William Mong Institute of Nano Science and Technology, and Center for Metamaterials Research, Hong Kong University of Science and Technology, Hong Kong, China*
[2]*Department of Electronic and Computer Engineering, Hong Kong University of Science and Technology, Hong Kong, China*
[3]*eekmlau@ust.hk*
[4]*phkswong@ust.hk*

Abstract: Nanolasers directly grown on silicon substrates are ideal light sources for silicon-based photonic integrated circuits, benefiting from an ultra-small footprint and ultra-low energy consumption. However, constructing a compact laser source that covers a wide emission range is still challenging, especially for data-communication applications in the near-infrared region. Here, we explain a wavelength tuning strategy for InP/InGaAs nano-ridge lasers grown on silicon-on-insulator wafers through experimental measurements and detailed simulations. A wide tuning range of over 200 nm is achieved via tailoring the length of the on-chip Fabry-Pérot nano-ridge lasers with identical epitaxial structures. With extensive mode and gain analyses of the nano-ridge lasers, we attribute the broadband tuning scheme to the enhanced band filling effect and the significant gain shift under high excitation levels. Our study provides a fresh perspective for the design of telecom nano-scale light emitters.

Si-based photonic integrated circuits (PICs) have been receiving extensive attention in opto-electronics, due to their ability to achieve high functionality and low-cost chips through mature CMOS processes [1]. An epitaxially-grown III-V light source is a desired building block for compact, scalable Si-based PICs [2,3]. Tunable on-chip lasers are of particular interest due to their potential applications in wavelength-division multiplexing (WDM) and realizing broadband PICs [4–6]. However, choices in up-to-date wide-range emitters are still very limited, especially in monolithic and compact near-infrared laser sources [7].

One strategy to control the wavelength of III-V lasers is to design laser cavities for precise mode selection. In one approach, the laser cavity's optical feedback comes from periodically arranged structures in the active region (distributed feedback (DFB) lasers), and the lasing wavelength is adjusted by tailoring the DFB laser parameters [5,8,9]. In another approach, the emission peak can be precisely manipulated by defining photonic crystal cavities [4]. Other tuning schemes based on selecting resonance modes include integrating double-ring resonators [10] and distributed Bragg reflectors (DBRs) [11] into the laser cavities. Although the lasing peak is precisely controlled under these schemes, the tunable range of the lasing wavelength is narrow (less than 70 nm). Moreover, the footprint and volume of these lasers are relatively large because of the introduction of external cavities. Another scheme to alter the lasing wavelength is to change the chemical composition or structure of the active region. For ternary III-V alloys such as InGaAs, the band gap can be changed from 0.36 eV to 1.4 eV by adjusting the indium composition. Wide-band lasing over 300 nm has been demonstrated in InGaAs/InGaP nano-beam lasers with different indium fractions [4]. Additionally, for III-V heterostructures such as InP/InGaAs, the emission peak also depends on the thickness of the InGaAs quantum well (QW) [12,13]. A

#369315 https://doi.org/10.1364/OSAC.2.003037
Journal © 2019 Received 5 Jun 2019; revised 2 Oct 2019; accepted 7 Oct 2019; published 22 Oct 2019

OSA CONTINUUM

broad lasing range of over 400 nm has recently been demonstrated in InP/InAs nanowire lasers with different InAs QW thicknesses [14]. However, tuning the lasing peak of this type of laser source requires different active regions and thus requires multiple epitaxy processes. Therefore, achieving a widely tunable telecom-range nanolaser with a single epitaxial structure is still a challenge.

Recently, we discovered a wide-band lasing behavior from InP/InGaAs nano-ridge lasers with identical InP/InGaAs QW active regions [15,16]. By defining the InP/InGaAs nano-ridge laser cavity into different lengths, the emission peak of the nano-ridge lasers spans over 200 nm from the O-band to the C-band. However, the origin of this behavior is still unclear. In this paper, we present a study of the relationship between the lasing wavelength and the nano-ridge laser cavity length, and unveil the underlying mechanism through extensive mode and gain analyses.

Figure 1(a) and (b) show the structural schematic and scanning electron microscopy (SEM) image of an InP/InGaAs nano-ridge laser array directly grown on (001) silicon-on-insulator (SOI) wafers using metal organic chemical vapor deposition. The growth and fabrication methods are detailed in our earlier works [15,17,18]. Five uniform and symmetric InGaAs QWs were embedded inside the InP nano-ridge as the active gain medium (see the inset of Fig. 1(b)). The average thickness of the InGaAs QWs was measured as 6 nm using cross-sectional transmission electron microscopy. The length of the nano-ridge lasers, defined using focused-ion beam (FIB) milling, varied from 25 µm to 80 µm. Room-temperature lasing was observed from the nano-ridges under optical pumping conditions. The nano-ridge laser features a broad spontaneous emission with evenly spaced Fabry-Pérot (FP) resonance peaks below the lasing threshold, and a strong peak at 1494 nm above the threshold (see Fig. 1(c)). Additionally, most of the measured nano-ridge lasers exhibited clean lasing spectra together with low lasing thresholds, suggesting that only a single transverse mode is amplified in our nano-ridge lasers.

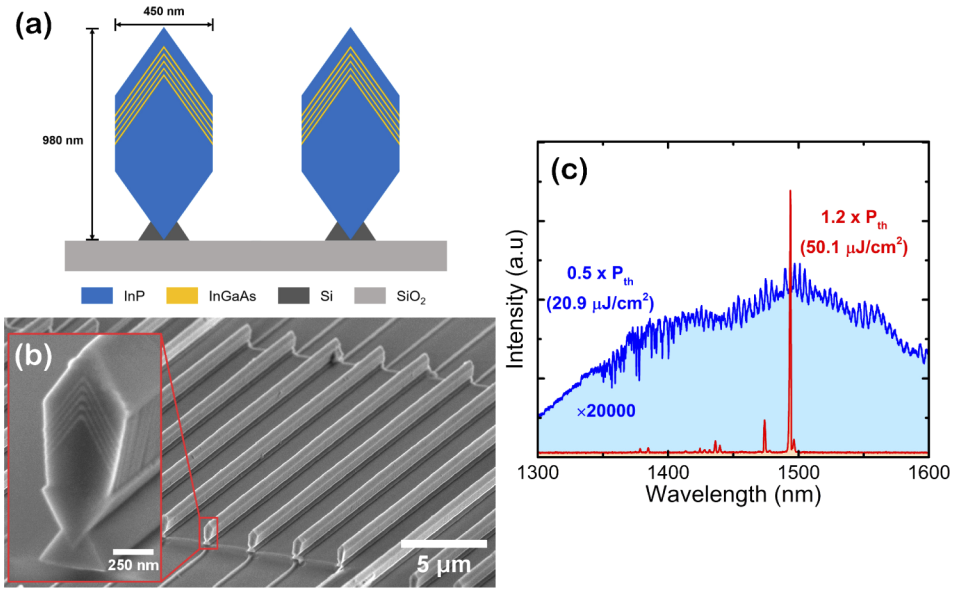

Fig. 1. (a) Schematic of the cross-section of the designed InP/InGaAs nano-ridge laser array grown on SOI substrate. (b) 70° tilted SEM image of nano-ridge lasers on SOI; the inset shows the zoomed-in image on the cross-section of the nano-ridge laser. (c) Room-temperature emission spectra of the 60 µm nano-ridge laser below (blue, magnified ×20000) and above (red) the lasing threshold (41.8 µJ/cm^2).

OSA CONTINUUM

A systematic measurement of the lasing wavelength with respect to the nano-cavity length is summarized in Fig. 2. An *S*-shaped wavelength versus cavity-length relationship is shown, with a turning point at 45 μm. Surprisingly, with identical InGaAs QWs as the active region, the lasing wavelengths can cover a range of over 200 nm from the O-band to the S-band, which is unexpected and approximately an order of magnitude greater than the tunable range in traditional InGaAs lasers [19]. Generally, a shorter lasing wavelength can be achieved via tailoring the nano-ridge laser to a shorter length. For the lasers shorter than 35 μm (Region A) and longer than 55 μm (Region C), lasing only arose at around 1350 nm and around 1500 nm, respectively. Both the long and short cavity length regions display a quasi-linear relationship with the lasing wavelength. It is noteworthy that a broad range of wavelengths from 1350 nm to 1500 nm can be supported at moderate lengths of about 40 μm to 50 μm (Region B). This unique phenomenon of wavelength dependence in the telecom region demonstrates broadband emission in a single epitaxial structure, which has yet to be observed in other lasers.

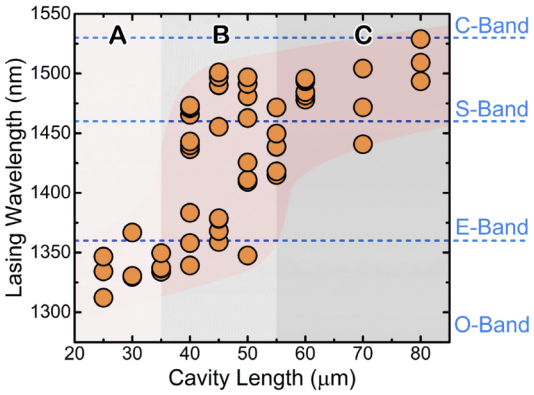

Fig. 2. Relationship between lasing wavelength and nano-ridge laser cavity length.

To understand the origin of the broadband lasing behavior, it is crucial to identify the lasing mode and study the modal reflectivity and confinement factors. Finite-difference eigenmode (FDE) and Finite-difference time-domain (FDTD) simulations were performed to investigate the mode characteristics of the nano-cavities. The first few modes are modeled at different mode wavelengths. The modes are guided in an infinitely long cavity with one end facet. Their group indices, confinement factors, and modal reflectivity are shown in Fig. 3. Note that the confinement factor is defined here as the proportion of electric field strength in the QWs to that of the whole transverse plane, with the energy velocity taken into account [20,21]. Interestingly, the TE_{01} mode possesses a remarkably high mode confinement factor in the active region and a large end-facet reflectivity across the whole gain spectrum, as illustrated in Figs. 3(b) and 3(c). These results suggest that the TE_{01} mode is most likely the dominant lasing mode in our nano-ridge lasers because of its uniquely strong feedback and high energy gain. It is worth noting that the fundamental modes HE_{11a} and HE_{11b} can also be supported, but they experience a significantly lower confinement and reflectivity, and are therefore unlikely to lase. Furthermore, the group index $n_g = 4.36$ is obtained at a wavelength of 1475 nm, according to the measurements of the free spectral range (FSR) below the lasing threshold (see Fig. 1(b)). This value corresponds well to the results in the FDE simulation as shown in Fig. 3(a), indicating that the observed mode is indeed the TE_{01} mode. We attribute the minute deviations in mode group index to the slight unevenness in size and shape of the supporting Si pedestals. Hence, we are confident that the TE_{01} mode is the only lasing mode supported in our lasers, regardless of the emission wavelength.

Lasing occurs when loss equates to gain ($g_m = \alpha_T$). Since the well-defined structure of the nano-ridges leads to strong feedback from the end facets, the nano-ridges can be treated as

OSA CONTINUUM

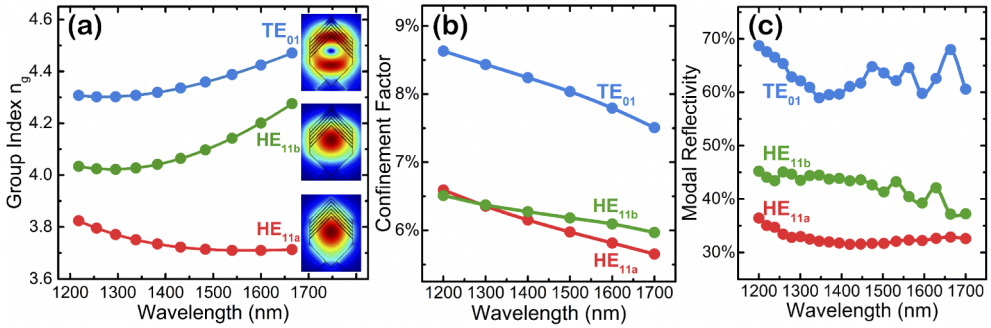

Fig. 3. (a) FDE simulation of the group index n_g of the first three eigenmodes in the nano-ridges at different mode wavelengths; the inset illustrates the profiles of the HE_{11a}, HE_{11b} and TE_{01} modes at 1400 nm. (b) Confinement factors of the modes in QW active layers at different mode wavelengths. (c) FDTD simulation of modal reflectivity at different mode wavelengths of the same three modes.

excellent FP resonators. The loss in FP lasers is mainly determined by mirror loss at the end facets, and intrinsic loss from defect sites. The total loss α_T in our lasers, hence, can be described as

$$\alpha_T = -\frac{1}{L}\ln(\tilde{R}) + \alpha_i \,, \tag{1}$$

where α_i and L are the intrinsic loss and cavity length of the nano-ridge laser, respectively, and $\tilde{R}$ is the geometric mean of the modal reflectivity at the end facets. Due to the ultra-low intrinsic loss in our lasers and the nearly flat, high reflectivity of the TE_{01} mode at different wavelengths (see Fig. 3(c)), the lasing threshold of our nano-ridge lasers is primarily controlled by cavity length. By truncating nano-ridges into different lengths via FIB milling, the inversely proportional relation between the lasing threshold and cavity length of the nano-ridge lasers is obtained (see Fig. 4(a)), which matches our expectations from Eq. (1). The simple connection between the length and loss of the lasers allows us to manipulate the loss by controlling the length of the nano-cavity.

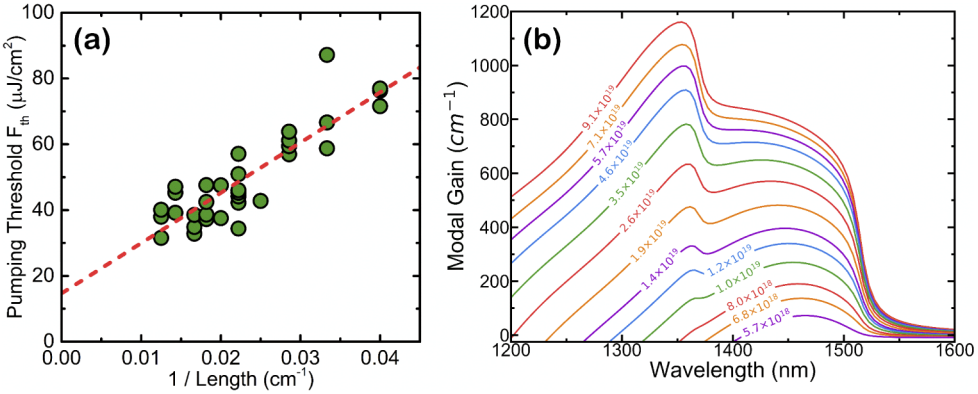

Fig. 4. (a) Relationship between the pumping threshold F_{th} and 1/length of the nano-ridge lasers. The linear relation is fitted using Eq. (1) according to the fact that the loss of the lasers α_T is directly proportional to the lasing threshold F_{th}. (b) Modal gain spectra of the InP/InGaAs QW active layer under different carrier densities. The carrier densities are indicated on the spectra in the unit of cm^{-3}.

OSA CONTINUUM

In addition, the wavelength-dependent peak modal gain from the QW active layer also affects the lasing peak. The modal gain spectrum of the TE_{01} mode in the InP/InGaAs nano-ridge lasers is calculated according to

$$g_{\mathrm{m}}(\omega) = \Gamma g(\omega) \tag{2}$$

where Γ and $g(\omega)$ are the mode confinement factor and material gain of the InP/InGaAs QWs. Note that, for simplicity, we only consider the lasing TE_{01} mode in the calculation, since the other modes experience much higher losses and less gain. The material gain $g(\omega)$ of the InP/InGaAs QW is calculated using the band-to-band radiative transitions model of electrons, described as [20,22],

$$g(\omega) = \frac{\pi e^2}{n\varepsilon_0 c m_0^2 \omega} \sum_{n_c,n_v} \int_0^\infty |M_T|^2 \left(\frac{m_r H}{\pi\hbar^2 d}\right)(f_c - f_v)\left(\frac{\hbar}{\pi\tau_{in}} \frac{1}{(E-\hbar\omega)^2 + (\hbar/\tau_{in})^2}\right) dE, \tag{3}$$

where e, n, ε_0, c, m_0, $\hbar$ and M_T are electron charge, material refractive index, permittivity of free space, speed of light in a vacuum, electron rest mass, reduced Planck constant and transition matrix element. The first parenthesis in the integral, with the Heaviside step function H, the reduced effective mass m_r and the QW thickness d, represents the density of states between two sub-bands of the QW system. f_c, f_v and τ_{in} are the Fermi-Dirac distribution functions of electrons and holes and the intra-band scattering lifetime of carriers, respectively. The summation in the equation takes into consideration all the possible transitions between the conduction sub-bands n_c and valence sub-bands n_v. Additional transition channels from the broadening of energy states are taken into account as the Lorentzian lineshape function in the last parenthesis of the integrand.

The modal gain spectra are calculated from the radiative transition model constructed according to Eqs. (2) and (3). Figure 4(b) displays the modal gain spectra of the InP/InGaAs QW, with a thickness of 6 nm, under various carrier densities. Owing to the consistently high confinement factors of the TE_{01} mode at different wavelengths, the modal gain spectrum shares a similar shape with the material gain spectrum. The modal gain spectra indicate that there is only a slight blue-shift at the relative low carrier densities ($n \leq 1.4 \times 10^{19}$ cm^{-3}), but at moderate to high carrier densities, the gain peak dramatically shifts to a shorter wavelength. The redistribution of energy states resulting from the quantum confinement effect forms discrete energy sub-bands in the QWs. With the reduced density of states in each sub-band, the band filling effect can be drastically enhanced [23]. As a result, the transitions between different energy sub-bands can bring the multiple peaks feature to the gain spectrum under reasonably low pumping levels (i.e. $n \sim 2 \times 10^{19}$ cm^{-3}). By slightly increasing the carrier density in the QWs, the peak gain position shifts from around 1460 nm to 1360 nm. This suggests the possibility of adjusting emission wavelength according to carrier density in nano-ridge lasers with low-dimensional active layers, such as the InP/InGaAs QWs described here. Rearranging the energy band structure in QW is crucial in gaining access to higher transition energy channels and thus covering a wider wavelength range, which bulk nanolasers cannot achieve.

To predict the lasing behavior of the nano-ridge lasers with various cavity lengths, the relationship between the emission wavelength and the length of the nano-ridge lasers is theoretically modeled. Figure 5 illustrates the normalized gain spectrum as a function of nano-ridge laser length. Since the length of the laser is implicitly included in the expression of the pumping threshold (see Fig. 4(a)), by extracting the relation between the carrier density and the peak wavelength from the gain spectra in Fig. 4(b), the peak emission wavelength and the laser cavity length can be correlated using

$$F_{th} = \frac{N_{th}\left(hc/\lambda\right) V_a}{\eta A_p}, \tag{4}$$

where F_{th}, N_{th}, λ, V_a, η and A_p are the threshold pumping fluence, average carrier density in the active layers at the lasing threshold, excitation wavelength, QW active layer volume, fraction of

OSA CONTINUUM

absorbed excitation power in a nano-ridge and pumping stripe area. As the cavity length decreases, the gain region transits from longer to shorter wavelengths. The lasing threshold also increases accordingly to compensate for the mirror loss. The peak gain is around 1360 nm in region A under high carrier densities, and 1460 nm in region C with low carrier densities. In contrast, the peak gain spans over 100 nm from 1360 nm and 1460 nm in region B with medium carrier densities. This model shows a wavelength transition behavior that agrees with our experimental result in Fig. 2. Moreover, it is interesting that in region B, the wavelength dependence of the gain becomes insignificant. This suggests the possibility of achieving telecom-broadband lasing with a single length of nano-ridge lasers under a reasonably low pumping intensity.

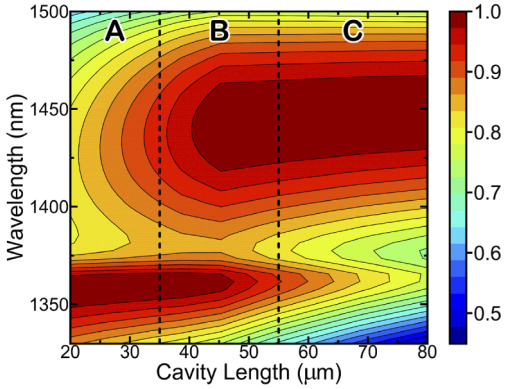

Fig. 5. Contour plot of the normalized modal gain spectrum of InP/InGaAs QW at 6 nm thickness.

Although a wide wavelength range of over 150 nm was expected in our calculations (assuming 90% or higher of the peak gain could compensate for the mirror loss, and thus lase), the experimentally observed emission range over 200 nm was still beyond our anticipation. We attribute the unexpectedly wide tuning range of the nano-ridge lasers to the inhomogeneity of the QW active layers. The slight variations in QW thickness from the epitaxy process induce additional gain spectrum broadening, resulting in a larger lasing wavelength range than expected. The wider distribution of transition energies from the QW thickness discrepancies also extends the overall lasing band. Hence, the emission range is outstretched and allows the lasing wavelength to span across the O-band to the S-band.

In conclusion, we have demonstrated a broadband lasing behavior via controlling the cavity length of InP/InGaAs nano-ridge lasers directly grown on SOI wafers and explained the underlying mechanism through detailed mode and gain calculations. The TE_{01} mode was identified to be the lasing mode due to the large confinement factor and strong feedback from the end facets. By simulating the modal gain and mirror loss of the TE_{01} mode, we predicted an *S*-shaped relationship between the emission peak and the cavity length that agrees well with our experimental data. This work suggests an interesting scheme for realizing broadband emission in laser sources with low-dimensional active regions, and provides a new perspective on constructing wide-range on-chip infrared emitters for data-communication applications.

Funding

Research Grants Council, University Grants Committee (16212115, 16245216, AoE/P-02/12); Innovation and Technology Fund (ITS/273/16FP); William Mong Institute of Nano Science and Technology (WMINST19/SC04).

OSA CONTINUUM

Acknowledgments

The authors would like to thank the MCPF and NFF of HKUST for their technical assistance.

Disclosures

The authors declare that there are no conflicts of interest related to this article.

References

1. F. Kish, V. Lal, P. Evans, S. W. Corzine, M. Ziari, T. Butrie, M. Reffle, H. Tsai, A. Dentai, J. Pleumeekers, M. Missey, M. Fisher, S. Murthy, R. Salvatore, P. Samra, S. Demars, N. Kim, A. James, A. Hosseini, P. Studenkov, M. Lauermann, R. Going, M. Lu, J. Zhang, J. Tang, J. Bostak, T. Vallaitis, M. Kuntz, D. Pavinski, A. Karanicolas, B. Behnia, D. Engel, O. Khayam, N. Modi, M. R. Chitgarha, P. Mertz, W. Ko, R. Maher, J. Osenbach, J. T. Rahn, H. Sun, K.-T. Wu, M. Mitchell, and D. Welch, "System-on-Chip Photonic Integrated Circuits," IEEE J. Sel. Top. Quantum Electron. **24**(1), 1–20 (2018).
2. J. E. Bowers and D. Liang, "Recent progress in lasers on silicon," Nat. Photonics **4**(8), 511–517 (2010).
3. Z. Wang, A. Abbasi, U. Dave, A. Groote, S. Kumari, B. Kunert, C. Merckling, M. Pantouvaki, Y. Shi, B. Tian, K. Gasse, J. Verbist, R. Wang, W. Xie, J. Zhang, Y. Zhu, J. Bauwelinck, X. Yin, Z. Hens, J. Campenhout, B. Kuyken, R. Baets, G. Morthier, D. Thourhout, and G. Roelkens, "Novel Light Source Integration Approaches for Silicon Photonics," Laser Photonics Rev. **11**(4), 1700063 (2017).
4. H. Kim, W. Lee, A. C. Farrell, A. Balgarkashi, and D. L. Huffaker, "Telecom-Wavelength Bottom-up Nanobeam Lasers on Silicon-on-Insulator," Nano Lett. **17**(9), 5244–5250 (2017).
5. Y. Shi, Z. Wang, J. Van Campenhout, M. Pantouvaki, W. Guo, B. Kunert, and D. Van Thourhout, "Optical pumped InGaAs/GaAs nano-ridge laser epitaxially grown on a standard 300-mm Si wafer," Optica **4**(12), 1468 (2017).
6. D. Thomson, A. Zilkie, J. E. Bowers, T. Komljenovic, G. T. Reed, L. Vivien, D. Marris-Morini, E. Cassan, L. Virot, J. Fédéli, J. Hartmann, J. H. Schmid, D. Xu, F. Boeuf, P. O'Brien, G. Z. Mashanovich, and M. Nedeljkovic, "Roadmap on silicon photonics," J. Opt. **18**(7), 073003 (2016).
7. R. Ma and R. F. Oulton, "Applications of nanolasers," Nat. Nanotechnol. **14**(1), 12–22 (2019).
8. Z. Wang, B. Tian, M. Pantouvaki, W. Guo, P. Absil, J. Van Campenhout, C. Merckling, and D. Van Thourhout, "Room-temperature InP distributed feedback laser array directly grown on silicon," Nat. Photonics **9**(12), 837–842 (2015).
9. B. Tian, Z. Wang, M. Pantouvaki, P. Absil, J. Van Campenhout, C. Merckling, and D. Van Thourhout, "Room Temperature O-band DFB Laser Array Directly Grown on (001) Silicon," Nano Lett. **17**(1), 559–564 (2017).
10. T. Chu, N. Fujioka, and M. Ishizaka, "Compact, lower-power-consumption wavelength tunable laser fabricated with silicon photonic-wire waveguide micro-ring resonators," Opt. Express **17**(16), 14063 (2009).
11. A. Fu, H. Gao, P. Petrov, and P. Yang, "Widely Tunable Distributed Bragg Reflectors Integrated into Nanowire Waveguides," Nano Lett. **15**(10), 6909–6913 (2015).
12. F. Lu, I. Bhattacharya, H. Sun, T. D. Tran, K. W. Ng, G. N. Malheiros-Silveira, and C. Chang-Hasnain, "Nanopillar quantum well lasers directly grown on silicon and emitting at silicon-transparent wavelengths," Optica **4**(7), 717 (2017).
13. F. Schuster, J. Kapraun, G. N. Malheiros-Silveira, S. Deshpande, and C. J. Chang-Hasnain, "Site-Controlled Growth of Monolithic InGaAs/InP Quantum Well Nanopillar Lasers on Silicon," Nano Lett. **17**(4), 2697–2702 (2017).
14. G. Zhang, M. Takiguchi, K. Tateno, T. Tawara, M. Notomi, and H. Gotoh, "Telecom-band lasing in single InP/InAs heterostructure nanowires at room temperature," Sci. Adv. **5**(2), eaat8896 (2019).
15. Y. Han, W. K. Ng, Y. Xue, Q. Li, K. S. Wong, and K. M. Lau, "Telecom InP/InGaAs nanolaser array directly grown on (001) silicon-on-insulator," Opt. Lett. **44**(4), 767 (2019).
16. Y. Han, W. K. Ng, C. Ma, Q. Li, S. Zhu, C. C. S. Chan, K. W. Ng, S. Lennon, R. A. Taylor, K. S. Wong, and K. M. Lau, "Room-temperature InP/InGaAs nano-ridge lasers grown on Si and emitting at telecom bands," Optica **5**(8), 918 (2018).
17. Y. Han, Q. Li, S. Chang, W. Hsu, and K. M. Lau, "Growing InGaAs quasi-quantum wires inside semi-rhombic shaped planar InP nanowires on exact (001) silicon," Appl. Phys. Lett. **108**(24), 242105 (2016).
18. Y. Han, Q. Li, K. W. Ng, S. Zhu, and K. M. Lau, "InGaAs/InP quantum wires grown on silicon with adjustable emission wavelength at telecom bands," Nanotechnology **29**(22), 225601 (2018).
19. J. N. Shapiro, A. Lin, P. S. Wong, A. C. Scofield, C. Tu, P. N. Senanayake, G. Mariani, B. L. Liang, and D. L. Huffaker, "InGaAs heterostructure formation in catalyst-free GaAs nanopillars by selective-area metal-organic vapor phase epitaxy," Appl. Phys. Lett. **97**(24), 243102 (2010).
20. L. A. Coldren, S. W. Corzine, and M. L. Mašanovitć, *Diode lasers and photonic integrated circuits* (Wiley, 2012).
21. D. Saxena, N. Jiang, X. Yuan, S. Mokkapati, Y. Guo, H. H. Tan, and C. Jagadish, "Design and Room-Temperature Operation of GaAs/AlGaAs Multiple Quantum Well Nanowire Lasers," Nano Lett. **16**(8), 5080–5086 (2016).
22. W. S. Ko, C. Chang-Hasnain, L. C. Chuang, F. G. Sedgwick, K. W. Ng, T. D. Tran, and R. Chen, "Nanolasers grown on silicon," Nat. Photonics **5**(3), 170–175 (2011).
23. Y. Arakawa and A. Yariv, "Quantum well lasers–Gain, spectra, dynamics," IEEE J. Quantum Electron. **22**(9), 1887–1899 (1986).